The Astrophysical Journal Letters, 969:L24 (10pp), 2024 July 1 https://doi.org/10.3847/2041-8213/ad5967

The Aligned Orbit of a Hot Jupiter around the M Dwarf TOI-4201

Tianjun Gan[1], Sharon X. Wang[1], Fei Dai[2], Joshua N. Winn[3], Shude Mao[1], Siyi Xu[4], Enric Pallé[5,6], Jacob L. Bean[7], Madison Brady[7], Nina Brown[7], Cicero Lu[4], Rafael Luque[7], Teo Mocnik[4], Andreas Seifahrt[4], and Guðmundur K. Stefánsson[8]
[1] Department of Astronomy, Tsinghua University, Beijing 100084, People's Republic of China; tianjungan@gmail.com
[2] Institute for Astronomy, University of Hawaii at Manoa, Honolulu, HI 96822, USA
[3] Department of Astrophysical Sciences, Princeton University, 4 Ivy Lane, Princeton, NJ 08544, USA
[4] Gemini Observatory/NSF NOIRLab, 670 N. A'ohoku Place, Hilo, HI 96720, USA
[5] Instituto de Astrofísica de Canarias (IAC), Vía Láctea s/n, E-38205 La Laguna, Tenerife, Spain
[6] Dept. Astrofísica, Universidad de La Laguna (ULL), E-38206 La Laguna, Tenerife, Spain
[7] Department of Astronomy & Astrophysics, University of Chicago, 5640 South Ellis Avenue, Chicago, IL 60637, USA
[8] Anton Pannekoek Institute of Astronomy, Science Park 904, University of Amsterdam, 1098 XH Amsterdam, The Netherlands
Received 2024 April 29; revised 2024 June 16; accepted 2024 June 18; published 2024 July 1

Abstract

Measuring the obliquities of stars hosting giant planets may shed light on the dynamical history of planetary systems. Significant efforts have been made to measure the obliquities of FGK stars with hot Jupiters, mainly based on observations of the Rossiter–McLaughlin effect. In contrast, M dwarfs with hot Jupiters have hardly been explored because such systems are rare and often not favorable for such precise observations. Here, we report the first detection of the Rossiter–McLaughlin effect for an M dwarf with a hot Jupiter, TOI-4201, using the Gemini-North/MAROON-X spectrograph. We find TOI-4201 to be well aligned with its giant planet, with a sky-projected obliquity of $\lambda = -3.0^{+3.7}_{-3.2}{}^{\circ}$ and a true obliquity of $\psi = 21.3^{+12.5}_{-12.8}{}^{\circ}$ with an upper limit of 40° at a 95% confidence level. The result agrees with dynamically quiet formation or tidal obliquity damping that realigned the system. As the first hot Jupiter around an M dwarf with its obliquity measured, TOI-4201b joins the group of aligned giant planets around cool stars ($T_{\rm eff} < 6250$ K), as well as the small but growing sample of planets with relatively high planet-to-star mass ratio ($M_p/M_* \gtrsim 3 \times 10^{-3}$) that also appear to be mostly aligned.

Unified Astronomy Thesaurus concepts: Planetary alignment (1243); Exoplanet dynamics (490); Star-planet interactions (2177); Exoplanets (498); M dwarf stars (982); Hot Jupiters (753)

1. Introduction

Since the first discovery of a hot Jupiter (Mayor & Queloz 1995), the origin of such short-period planets has been the subject of much research. Three basic hypotheses have been postulated: in situ formation, disk-driven migration, and high-eccentricity migration (Dawson & Johnson 2018). Unlike the other two scenarios, high-eccentricity migration would tend to excite inclinations through planet scattering (Rasio & Ford 1996; Chatterjee et al. 2008; Ford & Rasio 2008), Kozai–Lidov interactions (Fabrycky & Tremaine 2007; Naoz 2016), and secular resonances (Wu & Lithwick 2011; Petrovich et al. 2020). All these routes might be expected to result in misalignment between the planet's orbital angular momentum vector and the star's spin angular momentum vector (i.e., a large stellar obliquity). For this reason, measuring stellar obliquities is useful as a probe of the dynamical history of close-orbiting giant planets (see Albrecht et al. 2022, and references therein).

One way to determine the stellar obliquity is through the Rossiter–McLaughlin (RM) effect (McLaughlin 1924; Rossiter 1924), the distortion in the stellar spectral lines due to selective blockage of the star's rotating photosphere by a transiting planet. Unlike the Sun, for which the equatorial plane is tilted by only 7° from the ecliptic (Beck & Giles 2005), a significant fraction of hot-Jupiter hosts are found to be misaligned (Winn & Fabrycky 2015). In particular, relatively hot and massive stars ($T > 6250$ K, $M > 1.3\,M_{\odot}$) exhibit a broad range of spin–orbit angles, while cooler and less massive stars tend to be well aligned (Schlaufman 2010; Winn et al. 2010). The critical effective temperature separating these groups is close to the "Kraft break" (Kraft 1967) that separates stars with convective and radiative envelopes. Since cool stars have thicker and more massive convective envelopes than hot stars (Pinsonneault et al. 2001), and convective envelopes are thought to allow for more rapid tidal dissipation, Winn et al. (2010) speculated that many hot Jupiters once had misaligned orbits but tidal dissipation damped the obliquities and realigned the systems (see also Albrecht et al. 2012; Wang et al. 2021; Spalding & Winn 2022). If so, then one might expect hot Jupiters around M dwarfs to be especially well aligned since they have deep convective zones. One might also wonder whether late M dwarfs, which are fully convective, should allow for rapid tidal obliquity damping or if the absence of a radiative/convective boundary changes the situation.

There have been many recent studies of orbital misalignment of M dwarfs with nongiant planets, such as TRAPPIST-1 (Hirano et al. 2020a; Brady et al. 2023), GJ 436 (Bourrier et al. 2018), AU Mic (Hirano et al. 2020b; Martioli et al. 2020; Palle et al. 2020; Addison et al. 2021), K2-25 (Stefansson et al. 2020), GJ 3470 (Stefánsson et al. 2022), and K2-33 (Hirano et al. 2024). However, obliquity measurements for M dwarfs with hot Jupiters are lacking due mainly to the low occurrence rate of such systems (Gan et al. 2023a; Bryant et al. 2023). To our knowledge, Dai et al. (2018) made the first attempt to measure the obliquity of an M dwarf with a hot Jupiter, Kepler-45b.

Instead of using the RM effect, they studied the light-curve anomalies produced when a transiting planet crosses over starspots (Sanchis-Ojeda et al. 2011) and found an upper limit of 10° on the obliquity of the host star. With a similar methodology, recent works by Almenara et al. (2022) and Libby-Roberts et al. (2023) both found that TOI-3884, an M4 dwarf hosting a super-Neptune, is likely misaligned.

Further progress has been made possible by the full-sky photometric survey performed by NASA's Transiting Exoplanet Survey Satellite (TESS; Ricker et al. 2015), which has led to the enlargement of the sample of M dwarfs with hot Jupiters. Alongside this development is the advent of a new generation of high-resolution stabilized spectrographs on large telescopes. Together, these advances provide an opportunity to extend obliquity studies to M dwarfs with giant planets. Here, we present the first measurement of the RM effect for a hot Jupiter transiting an M dwarf, TOI-4201b. The star is an early M dwarf at a distance about 189 pc, and it hosts a hot Jupiter with an orbital period of 3.58 days (Gan et al. 2023b; Hartman et al. 2023; Delamer et al. 2024). The rest of this Letter is organized as follows: Section 2 details the spectroscopic observations, Section 3 presents the joint-fit analysis, Section 4 discusses the results, and Section 5 describes our conclusions.

2. MAROON-X Spectroscopic Observations

Since the host star is faint ($V = 15.3$ and $J = 12.3$) and the transit duration is relatively short (~2 hr), high-resolution spectroscopic instruments on large telescopes are required to achieve high radial-velocity (RV) precision in a short amount of time while having enough sampling. We collected 19 spectra with an exposure time of 900 s on UT 2023 December 26 using MAROON-X under the program GN-2023B-FT-107, covering a full transit and a total of 3 hr outside of the transit. MAROON-X is a high-resolution ($R \sim 85{,}000$) optical fiber-fed echelle spectrograph installed on the 8.1 m Gemini North Telescope, on Maunakea, Hawaii, with a wavelength range from 500 to 920 nm (Seifahrt et al. 2018, 2020). During the observations, the air mass varied between 1.2 and 1.8, the sky was clear, and the seeing was around 0.″4 but degraded to 0.″7 after egress. The signal-to-noise ratio (SNR) per resolution element near the $H\alpha$ line (Order 93) is about 19 at the beginning but decreases to 14 after egress due to degraded seeing.

The raw MAROON-X data were reduced with custom Python 3 routines based on routines originally written for the CRIRES instrument (Bean et al. 2010). We then utilized the Spectrum Radial Velocity Analyzer (SERVAL; Zechmeister et al. 2018) pipeline to measure the RVs based on the template-matching method. We separately obtained RV estimates from the blue (500–670 nm) and red (650–920 nm) arms of the spectrograph, after correcting the main instrumental drift, and we treated these two RV time series as though they were from two different instruments. We converted all the time stamps of our measurements from Julian Date (JD) to Barycentric Julian Date (BJD) (Eastman et al. 2010). In addition to the RVs, we extracted stellar activity diagnostics including the chromatic RV index (CRX), the differential line width (dLW), and the Hα activity indices (Zechmeister et al. 2018). Both the red and blue arms captured the Hα line, allowing for independent measurements. Table A1 gives all of the results. The median uncertainties of the RVs from the blue and red arms are 4.5 and 4.6 m s^{-1}, respectively.

To rule out the possibility that short-term stellar activity (i.e., flares) mimic the RM signal, we examined the correlation between the activity indices and the apparent RVs, quantified by the Pearson correlation coefficient. We found no evidence for significant correlations ($p < 0.05$).

3. Analysis

We employed the Allesfitter code (Günther & Daylan 2021) to measure the sky-projected spin–orbit angle (λ) for TOI-4201b. We performed a joint fit of two TESS light curves from Sectors 06 and 33 with cadences of 30 and 10 minutes; eight ground-based light curves from LCOGT, MuSCAT, and SPECULOOS, publicly available on ExoFOP;[9] RV data drawn from the literature; and our RM measurements. The TESS light curves are adopted from Gan et al. (2023b), which were extracted through simple aperture photometry. The out-of-transit RVs were from CFHT/SPIRou (Gan et al. 2023b), Keck/HIRES (Hartman et al. 2023), WIYN/NEID, and Magellan/Planet Finder Spectrograph (PFS) (both from Delamer et al. 2024).

The joint model has ten key parameters: orbital period (P), mid-transit time (T_0), planet-to-star radius ratio (R_p/R_*), sum of radii divided by the orbital semimajor axis ($(R_p + R_*)/a$), cosine of the orbital inclination ($\cos i_p$), RV semiamplitude (K), eccentricity parameters ($\sqrt{e}\cos\omega$ and $\sqrt{e}\sin\omega$), sky-projected spin–orbit angle (λ), and projected rotational velocity ($v \sin i$). Moreover, we allowed for a light dilution factor[10] for the TESS data due to the large pixel scale (21″ pixel^{-1}). This was not necessary for the ground-based observations, for which TOI-4201 was well resolved. We adopted a quadratic limb-darkening law for the TESS photometry and a linear law for the ground-based data (Kipping 2013). The simpler linear law was adopted for the ground-based data because the amount of data from each instrument and the SNR was limited compared with TESS. For each photometric and spectroscopic data set, we allowed for a baseline offset and a "jitter" term to account for unmodeled sources of white noise. Uniform priors were placed on all parameters except for the TESS dilution factor, for which we set a truncated normal prior.

We performed an affine-invariant Markov Chain Monte Carlo analysis with 140 walkers to sample the posterior distributions of all parameters. A total of 150,000 steps were taken by each walker, and the first 30,000 "burn-in" steps were excluded. All Markov chains were run for more than 30 times their autocorrelation length so that the convergence was reached (Foreman-Mackey et al. 2013). Figure 1 and Table 1 summarize the main results. Among the results, we obtained $\lambda = -3.0^{+3.7}_{-3.2}$ °, indicating a good alignment. The ground-based light curves along with the best-fit transit models are presented in Figure 2. The posteriors of other relevant parameters are shown in Table B1 of the Appendix.

Based on the periodogram analysis for TESS data and ground-based long-term light curves from the Zwicky Transient Facility (Bellm et al. 2019; Masci et al. 2019), Gan et al. (2023b) reported that TOI-4201 shows a 17.3 ± 0.4 day photometric modulation, which is likely to be from stellar rotation. Assuming this is the case, and neglecting the effects of differential rotation, the stellar equatorial rotation velocity

[9] https://exofop.ipac.caltech.edu/tess/

[10] $D = F_C/(F_T + F_C)$, where F_T and F_C represent the target and contamination fluxes.

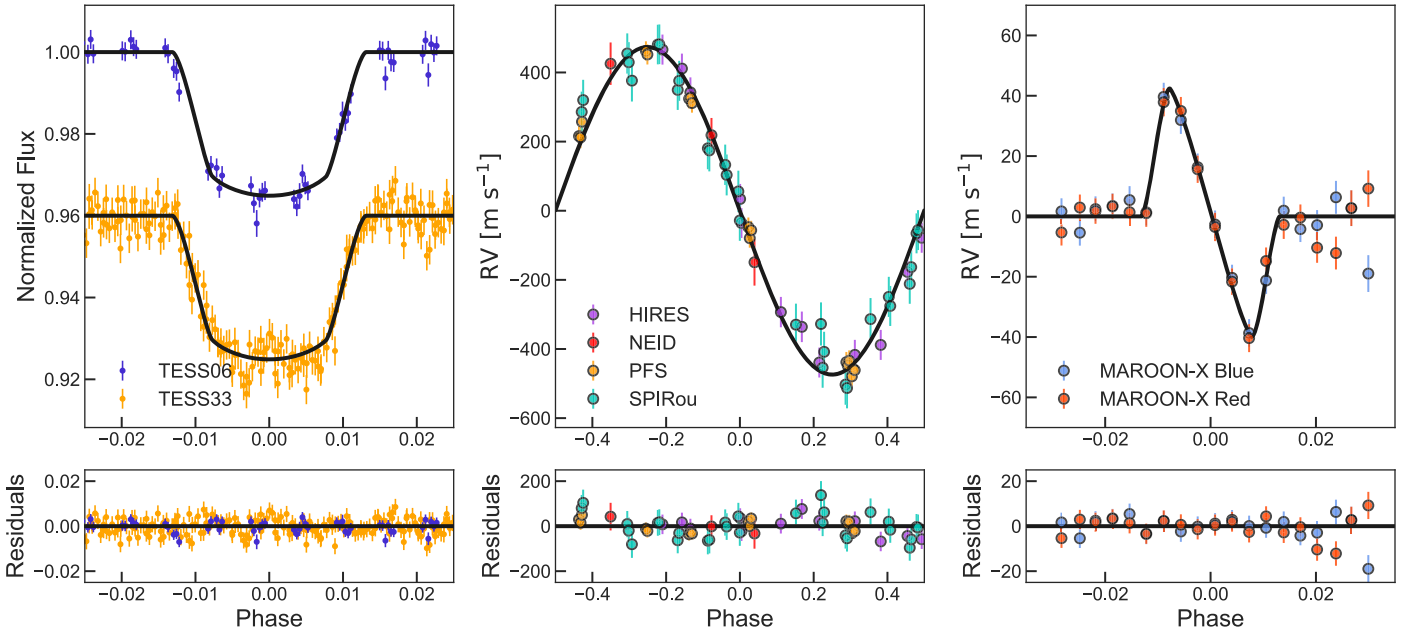

Figure 1. TESS transit photometry of TOI-4201 from Sectors 06 and 33 (left), out-of-transit RVs (middle), and RM measurements after subtracting the best-fit Keplerian model (right). The excess scatter in the RVs after egress is probably due to the degraded seeing. In each case, the black curve illustrates the best-fit model. The plotted error bars are the quadrature sums of the formal measurement uncertainties and the fitted "jitter" parameters. Residuals are shown in the bottom panels.

Table 1
Parameter Priors and Best Fits in the Joint Model for TOI-4201

Parameter	Prior	Best Fit	Description
Stellar Parameters[a]			
M_* ($M_\odot$)	...	0.61 ± 0.02	Stellar mass
R_* ($R_\odot$)	...	0.63 ± 0.02	Stellar radius
$T_{\rm eff}$ (K)	...	3794 ± 79	Stellar effective temperature
$\log g_*$ (cgs)	...	4.64 ± 0.03	Stellar surface gravity
$P_{\rm rot}$ (days)	...	17.3 ± 0.4	Stellar rotation period
Key Fitted Parameters			
P (days)	$\mathcal{U}$ (3.0, 4.0)	$3.5819198^{+0.0000013}_{-0.0000012}$	Orbital period
T_0 (BJD-2457000)	$\mathcal{U}$ (1470.93, 1470.99)	$1470.9618^{+0.0004}_{-0.0003}$	Mid-transit time
R_p/R_*	$\mathcal{U}$ (0.0, 0.5)	$0.1949^{+0.0013}_{-0.0012}$	Planet-to-star radius ratio
$(R_p + R_*)/a$	$\mathcal{U}$ (0.0, 0.5)	$0.0890^{+0.0015}_{-0.0013}$	Sum of radii divided by the orbital semimajor axis
$\cos i_p$	$\mathcal{U}$ (0.0, 1.0)	$0.0361^{+0.0025}_{-0.0023}$	Cosine of the orbital inclination
$\sqrt{e}\cos\omega$	$\mathcal{U}$ (−1, 1)	$-0.045^{+0.076}_{-0.066}$	Parameterization for e and ω
$\sqrt{e}\sin\omega$	$\mathcal{U}$ (−1, 1)	$-0.076^{+0.083}_{-0.071}$	Parameterization for e and ω
K (m s^{-1})	$\mathcal{U}$ (0, 1000)	$478.5^{+6.7}_{-7.1}$	RV semiamplitude
$v \sin i$ (km s^{-1})	$\mathcal{U}$ (0.1, 10)	$1.65^{+0.11}_{-0.09}$	Projected stellar rotation velocity
λ (deg)	$\mathcal{U}$ (−180, 180)	$-3.0^{+3.7}_{-3.2}$	Projected spin–orbit angle
Derived Stellar Parameters			
$i_\star$ (deg)	...	$67.4^{+14.3}_{-12.8}$	Stellar inclination
ψ (deg)	...	$21.3^{+12.5}_{-12.8}$	True obliquity
Derived Planetary Parameters			
R_p (R_J)	...	$1.19^{+0.04}_{-0.05}$	Planet radius
M_p (M_J)	...	$2.59^{+0.10}_{-0.11}$	Planet mass
a (AU)	...	$0.0398^{+0.0020}_{-0.0022}$	Semimajor axis
i_p (deg)	...	$87.9^{+0.2}_{-0.2}$	Orbital inclination
e	...	$0.008^{+0.026}_{-0.007}$	Orbital eccentricity
$T_{\rm eq}$[b] (K)	...	728^{+48}_{-44}	Equilibrium temperature

Notes. $\mathcal{U}$(a, b) stands for a uniform prior between a and b.
[a] The stellar parameters are adopted from Gan et al. (2023b).
[b] We do not consider heat distribution between the dayside and nightside here and assume albedo $A_B = 0$.

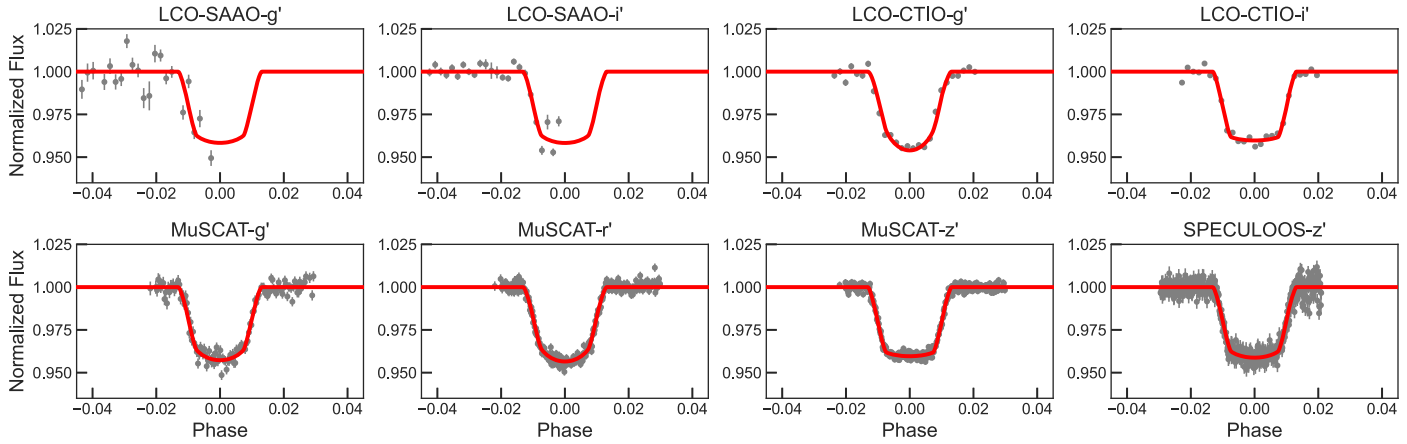

Figure 2. Dimensionless, phase-folded, ground-based transit observations of TOI-4201 with maximum phase of 1. The instrument name and observation filter are shown at the top of each panel. The red solid lines represent the best-fit transit models from the joint-fit analysis.

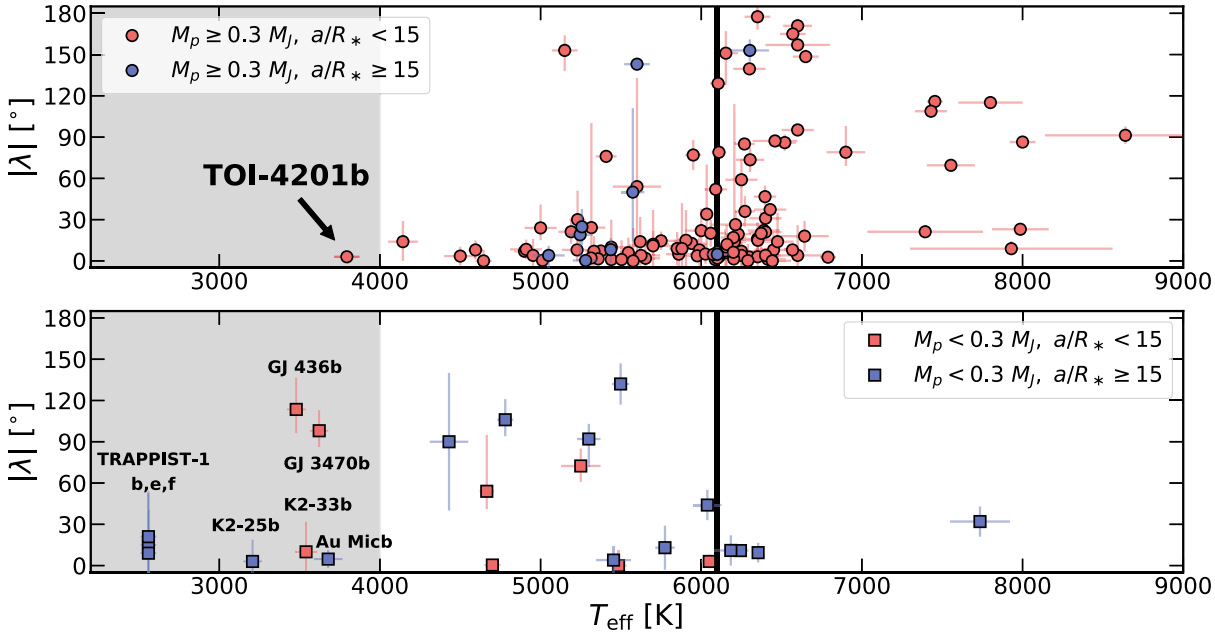

Figure 3. Top panel: projected stellar obliquity λ of giant-planet systems ($M_p \geqslant 0.3\ M_J$) versus host star effective temperature. Obliquity results are from RM measurements. The red dots are hot Jupiters (defined as having $a/R_\star < 15$), and the blue dots are warm Jupiters ($a/R > 15$). The position of TOI-4201b is marked with an black arrow. Bottom panel: same but for planets with $M_p < 0.3\ M_J$. In both panels, the vertical black line marks the Kraft break. The gray shaded region highlights the stars with $T_{\rm eff} \leqslant 4000$ K. Results were retrieved from the NASA Exoplanet Archive (Akeson et al. 2013).

$v = 2\pi R_*/P_{\rm rot} = 1.8 \pm 0.2$ km s^{-1}, which is consistent with the measured value of $v \sin i = 1.65^{+0.11}_{-0.09}$ km s^{-1} within about 1σ. Thus, there is no strong evidence for the difference between the stellar inclination and the orbital inclination angles. Nevertheless, we used the Bayesian inference methodology proposed by Masuda & Winn (2020) to place a quantitative constraint on $i_\star$, based on the likelihood function

$$\mathcal{L} = \left(\frac{R_*/R_\odot - 0.63}{0.02}\right)^2 + \left(\frac{P_{\rm rot} - 17.3\ \text{days}}{0.4\ \text{days}}\right)^2 + \left(\frac{v\sqrt{1-\cos^2 i_\star} - 1.6\ \text{km s}^{-1}}{0.2\ \text{km s}^{-1}}\right)^2. \quad (1)$$

We set uniform priors on R_* ($0 \leqslant R_* \leqslant 10\,R_\odot$), $P_{\rm rot}$ ($0 \leqslant P_{\rm rot} \leqslant 100$ days), and the cosine of stellar inclination $\cos i_\star$ ($0 \leqslant \cos i_\star \leqslant 1$) and sampled the parameter space using `emcee` (Foreman-Mackey et al. 2013). We initialized 150 walkers that each took 50,000 steps and discarded the first 5000 samples. We obtained a posterior of $\cos i_\star = 0.38^{+0.19}_{-0.24}$, or a stellar inclination of $i_\star = 67.4^{+14.3\circ}_{-12.8}$. The 3D obliquity ($\psi$) of TOI-4201 is then determined via (Albrecht et al. 2022)

$$\cos\psi = \cos i_\star \cos i_p + \sin i_\star \sin i_p \cos\lambda. \quad (2)$$

We used the posteriors of $i_\star$, i_p, and λ from the analysis above to obtain the true obliquity. The resulting true obliquity is $\psi = 21.3^{+12.5\circ}_{-12.8}$ with a 95% confidence that $\psi \leqslant 40°$, indicating that the system is aligned.

4. Discussion

4.1. The Dynamical History of TOI-4201b

TOI-4201b is one of the most massive hot Jupiters known to exist around an M dwarf. The planet's mass of $2.59^{+0.10}_{-0.11}\ M_J$ is

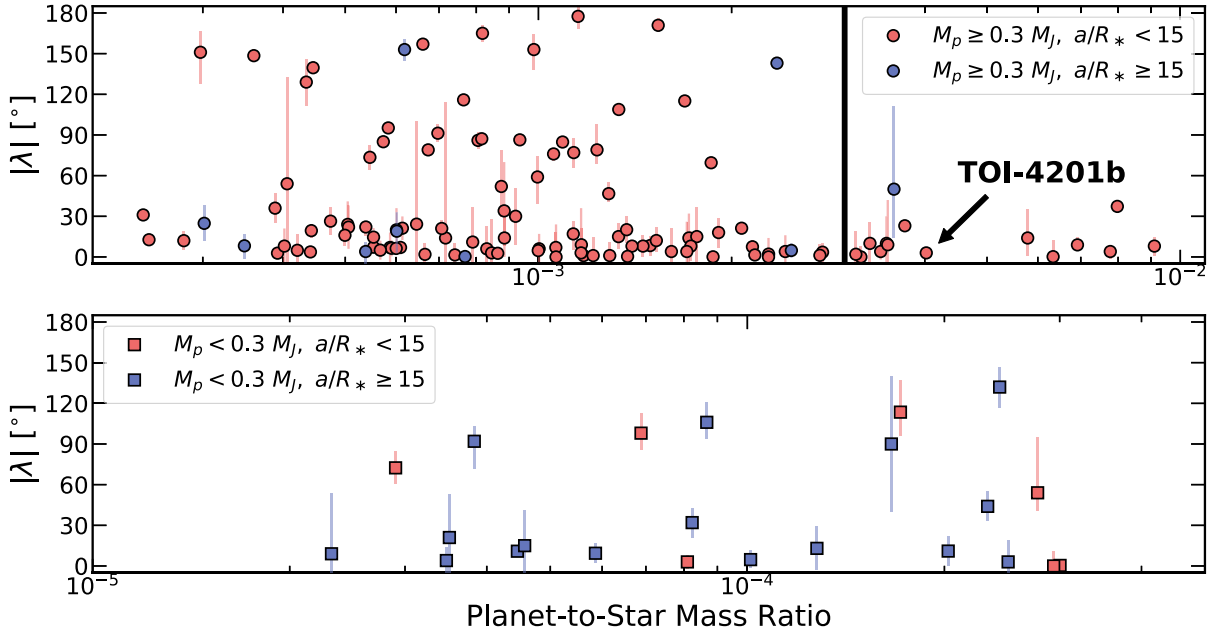

Figure 4. Projected stellar obliquity λ versus planet-to-star mass ratio, for four planet groups. Obliquity results are from RM measurements. Different colors represent planets with different scaled semimajor axes a/R_*. Giant-planet systems with mass ratio M_p/M_* over 3×10^{-3} (black vertical line) tend to be aligned, while small planets have a broad range of λ across mass ratio between 2×10^{-5} and 3×10^{-4}. The position of TOI-4201b is marked with a black arrow.

about 5 times heavier than the other known systems ($\sim$0.5 M_J). Therefore, the dynamical history of TOI-4201b may be different than those of previously studied systems.

A collision between two planets leading to a merger could account for the high mass but might tend to misalign the orbit relative to the star (Chatterjee et al. 2008), whereas we have found TOI-4201b to be well aligned. The good alignment might be the result of a more quiescent history or of tidal obliquity damping following any excitation. Likewise, the planet's low orbital eccentricity argues against high-eccentricity migration unless tidal eccentricity damping has erased the evidence.

As a simple estimate of the tidal realignment timescale $\tau_{\rm CE}$, we used the equation given by Zahn (1977):

$$\tau_{\rm CE} = 10\ {\rm Gyr}\left(\frac{M_p}{M_*}\right)^{-2}\left(\frac{a/R_*}{40}\right)^{6}, \quad (3)$$

where M_p/M_* is the planet-to-star mass ratio and a/R_* represents the semimajor axis in units of the stellar radius (see also Albrecht et al. 2012). We note that this scaling relation is calibrated using stellar binaries with an assumption that planetary systems have a similar process. With this in mind, we obtain a $\tau_{\rm CE} \approx 950$ Gyr using the updated physical parameters from the joint fit. The realignment timescale is much longer than any astrophysical timescale; thus, the stellar obliquity is not expected to significantly change after the planet was born. In addition to the dynamical tidal effect timescale above, we also derive the timescale of equilibrium tides using Equation (2) in Lai (2012). Adopting a reduced tidal quality factor Q' between 10^6 and 10^8 (Brown et al. 2011), we find that the $\tau_{\rm CE,eq}$ ranges from 2 to 200 Gyr, which is likely beyond the stellar age 0.7–2.0 Gyr estimated by Gan et al. (2023b) based on the empirical age–rotation relations (Barnes 2007; Mamajek & Hillenbrand 2008; Engle & Guinan 2018).

Next, we compute the ratio between the rotational angular momentum of the stellar convective layer and the planet's orbital angular momentum to evaluate whether the planet has the capability to realign the host star. The rotational angular momentum of the stellar convective layer is defined as

$$L_{\rm conv} = \frac{2\pi}{P_{\rm rot}} \times \kappa M_{\rm conv} R_*^2, \quad (4)$$

where $\kappa M_{\rm conv} R_*^2$ is the moment of inertia with κ depending on the stellar structure and $M_{\rm conv}$ represents the mass of the stellar convective layer. The planet orbital angular momentum is calculated through

$$L_p = \sqrt{GM_* M_p^2 a(1-e^2)}\cos i_p, \quad (5)$$

where M_* and M_p are the stellar and planet masses, a is the semimajor axis, and e and i_p represent the orbital eccentricity and inclination. According to the stellar models built by Pinsonneault et al. (2001), we find that TOI-4201 has a convective zone mass $M_{\rm conv}$ of about 0.1 $M_\odot$. Taking κ ranging from 0.1 to 0.2 (Baraffe et al. 2015), we obtain an angular momentum ratio $L_{\rm conv}/L_p$ between 0.15 and 0.3, indicating that TOI-4201b may be able to realign the star. To summarize, TOI-4201b has enough angular momentum to realign the spin axis of its host star before being destroyed by tidal decay, but the estimated timescale for realignment is longer than the estimated age of the system though we note that the timescale estimations both have large uncertainties. Our results suggest that a dynamical quiet history of TOI-4201b is more likely.

Previous studies on hot Jupiters around FGK stars suggest that tidal obliquity damping is negligible for planets with $a/R_* \geqslant 10$ (Albrecht et al. 2022). By this standard, TOI-4201 (with $a/R_* \approx 13.6$) is not expected to be affected significantly by tidal effects and would have preserved any initial misalignment. The well-aligned orbit of TOI-4201b hints that the limit of $a/R_* = 10$ on FGK stars may not be the same for M

dwarfs. The scaled semimajor axis boundary of strong and weak tidal obliquity damping for M dwarfs is possibly farther away ($a/R_* > 10$). On the other hand, however, TOI-4201 is less massive than FGK stars, making it easier to be realigned. At this point, we are not able to conclude the role tidal damping plays in this system. More such measurements on M dwarfs are required to figure out the tidal effect on different planetary systems.

4.2. TOI-4201b in the Broader Context

Figure 3 compares the stellar effective temperature and sky-projected obliquities of four types of planetary systems, differing in whether the planet is "hot" or "warm" and whether the planet is a giant or not. The boundary for these categorizations were $a/R_* = 15$ and $M_p = 0.3\,M_J$, which are chosen somewhat arbitrarily. We note that we did not put any restrictions on the stellar types here.

For the giant planets, we recover the known results that hot Jupiters around hot stars show a broader range of obliquities than those around cool stars with effective temperature $T_{\rm eff} < 6250$ K (Winn et al. 2010; Albrecht et al. 2012). Our observation of TOI-4201b has extended the domain of spin–orbit angle studies to include a Jupiter-like planet around an M dwarf. The result is in agreement with the previous findings. The behavior of small-planet systems seems more complicated. Below the Kraft break, several low-mass planets are found on nearly polar orbits (e.g., HAT-P-11b, Sanchis-Ojeda & Winn 2011; WASP-107b, Dai & Winn 2017; Rubenzahl et al. 2021; HD 3167c, Dalal et al. 2019; Bourrier et al. 2021; GJ 436b, Bourrier et al. 2018; GJ 3470b, Stefànsson et al. 2022). In fact, short-period small planets around M dwarfs that have deep convective envelopes tend to have a wide range of obliquity, similar to FGK counterparts.

In terms of planet-to-star mass ratio, Hébrard et al. (2011) reported that misaligned systems such as retrograde ones usually do not involve the most massive planets. Such a correlation still exists around stars with $T_{\rm eff} \leqslant 7000$ K but disappears around hotter stars when the sample is doubled (Albrecht et al. 2022). Figure 4 displays the 2D distributions of λ and mass ratio M_p/M_* of four planet groups. With a mass ratio of about 0.4%, TOI-4201b is located in the high-mass-ratio region where there are relatively few data points. Based on the figure, it seems that Jupiter-like planets with $M_p/M_* \gtrsim 3 \times 10^{-3}$ prefer aligned orbits although we note that the sample is limited. The stellar obliquities of small-planet systems, however, seem to have weak dependence on the mass ratio. Combining the giant- and small-planet samples, it turns out that the obliquities of planetary systems are mixed below a certain planet-to-star mass ratio. More observations on high-mass-ratio systems are required to draw a firm conclusion.

5. Conclusions

We reported the MAROON-X spectroscopic observations of a transit of TOI-4201b and determined that the planet's orbit is well aligned with the host star's spin axis with a sky-projected obliquity of $\lambda = -3.0^{+3.7}_{-3.2}{}^\circ$. Coupled with an estimate of the stellar rotation period, we found the true obliquity to be $\psi = 21.3^{+12.5}_{-12.8}{}^\circ$ with an upper limit of 40° at a 95% confidence level, suggesting either a dynamically cold formation history or tidal obliquity damping. TOI-4201b is the first hot Jupiter orbiting an M dwarf for which the obliquity has been measured via the RM effect. This observation extends the spin–orbit alignment studies of Jupiter-like planets from FGK to M dwarfs.

We further study TOI-4201b in the context of other systems with measured obliquities. We find that it is consistent with previous findings that hot-Jupiter hosts with $T_{\rm eff} < 6250$ K tend to have low obliquities. In addition, TOI-4201b joins the small but growing group of high-mass-ratio and aligned systems. Planetary systems with mass ratio $\gtrsim 3 \times 10^{-3}$ seem to prefer aligned orbits.

Acknowledgments

We thank Xianyu Wang for useful discussions and the anonymous referee for the comments that improved the quality of this Letter. This work is partly supported by the National Science Foundation of China (grant No. 12133005). T.G. acknowledges the Tsinghua Astrophysics High-Performance Computing platform at Tsinghua University for providing computational and data storage resources that have contributed to the research results reported within this Letter. E.P. acknowledges financial support from the Agencia Estatal de Investigación of the Ministerio de Ciencia e Innovación MCIN/AEI/10.13039/501100011033 and the ERDF "A way of making Europe" through project PID2021-125627OB-C32, and from the Center of Excellence "Severo Ochoa" award to the Instituto de Astrofisica de Canarias.

The University of Chicago group acknowledges funding for the MAROON-X project from the David and Lucile Packard Foundation, the Heising-Simons Foundation, the Gordon and Betty Moore Foundation, the Gemini Observatory, and the NSF (award number 2108465).

Based on observations obtained at the international Gemini Observatory, a program of NSF NOIRLab, which is managed by the Association of Universities for Research in Astronomy (AURA) under a cooperative agreement with the U.S. National Science Foundation on behalf of the Gemini Observatory partnership: the U.S. National Science Foundation (United States), National Research Council (Canada), Agencia Nacional de Investigación y Desarrollo (Chile), Ministerio de Ciencia, Tecnología e Innovación (Argentina), Ministério da Ciência, Tecnologia, Inovações e Comunicações (Brazil), and Korea Astronomy and Space Science Institute (Republic of Korea).

This work was enabled by observations made from the Gemini North telescope, located within the Maunakea Science Reserve and adjacent to the summit of Maunakea. We are grateful for the privilege of observing the Universe from a place that is unique in both its astronomical quality and its cultural significance.

Facilities: Gemini-North/MAROON-X, TESS, Keck/HIRES, WIYN/NEID, Magellan/PFS, CFHT/SPIRou, LCOGT, OAO: 1.88m.

Software: Allesfitter (Günther & Daylan 2021), emcee (Foreman-Mackey et al. 2013).

Appendix A
Spectroscopic Data Obtained for TOI-4201 with MAROON-X

We present the RVs and activity indicators including CRX, dLW, and $S_{\rm H\alpha}$ extracted with `SERVAL` (Zechmeister et al. 2018) in Table A1.

Table A1
Radial Velocities and Stellar Activity Indices for TOI-4201 Collected with MAROON-X in This Work

BJD	RV ($m\,s^{-1}$)	σ_{RV} ($m\,s^{-1}$)	CRX	CRXerr	dLW	dLWerr	$S_{H\alpha}$	$S_{H\alpha}$err
MAROON-X Blue								
2460304.803376	81.49	4.29	−92.46	62.46	21.94	7.67	0.56	0.01
2460304.815858	64.21	4.25	56.85	65.47	14.53	7.61	0.55	0.01
2460304.826498	63.31	4.18	26.68	53.71	10.25	7.48	0.57	0.01
2460304.838082	54.83	4.15	−12.55	49.57	27.16	7.42	0.56	0.01
2460304.849669	47.21	4.58	−105.69	80.20	34.24	8.21	0.55	0.01
2460304.861004	33.78	4.45	23.22	53.74	20.13	7.99	0.55	0.01
2460304.872871	62.24	4.63	−143.41	83.44	−8.68	8.35	0.54	0.01
2460304.884524	44.89	4.55	−85.99	70.29	27.17	8.14	0.58	0.01
2460304.895956	19.79	4.50	89.52	54.11	24.90	8.05	0.56	0.01
2460304.907782	−9.03	4.61	133.04	83.74	30.56	8.23	0.56	0.01
2460304.919321	−36.27	4.30	−70.71	69.76	28.40	7.68	0.54	0.01
2460304.930921	−64.20	4.58	156.22	77.01	22.85	8.21	0.54	0.01
2460304.942455	−56.35	4.39	15.18	79.36	−2.49	7.90	0.55	0.01
2460304.954451	−43.10	4.59	−27.47	55.60	28.76	8.23	0.55	0.01
2460304.965784	−58.58	4.24	8.58	82.19	3.47	7.61	0.54	0.01
2460304.977139	−66.62	4.96	−89.77	68.64	44.29	8.87	0.56	0.01
2460304.989955	−67.93	5.42	−12.89	86.10	50.25	9.66	0.53	0.01
2460305.000413	−80.07	5.93	92.30	72.43	67.84	10.53	0.56	0.01
2460305.011955	−111.20	6.07	251.34	93.57	88.95	10.76	0.55	0.02
MAROON-X Red								
2460304.803376	71.89	4.32	1.46	53.29	31.38	7.09	0.59	0.01
2460304.815858	69.97	4.29	19.31	55.58	42.28	7.02	0.58	0.01
2460304.826498	60.06	4.22	46.96	52.14	20.67	6.91	0.59	0.01
2460304.838082	52.06	4.19	6.83	60.75	29.48	6.89	0.59	0.01
2460304.849669	40.59	4.59	−55.61	55.97	28.89	7.56	0.56	0.01
2460304.861004	30.89	4.51	21.98	59.35	11.36	7.46	0.59	0.01
2460304.872871	57.89	4.68	61.01	60.34	7.27	7.75	0.62	0.02
2460304.884524	45.32	4.64	−53.73	77.62	14.03	7.68	0.61	0.02
2460304.895956	16.50	4.51	−65.55	48.81	18.67	7.44	0.58	0.01
2460304.907782	−12.43	4.69	−22.05	74.27	40.85	7.69	0.56	0.02
2460304.919321	−40.13	4.39	−57.66	59.70	23.03	7.24	0.59	0.01
2460304.930921	−68.48	4.64	9.85	48.60	10.45	7.68	0.59	0.02
2460304.942455	−52.46	4.48	−88.21	60.17	10.12	7.44	0.58	0.01
2460304.954451	−50.40	4.67	24.16	71.68	25.09	7.72	0.60	0.02
2460304.965784	−57.35	4.34	16.28	79.69	29.56	7.19	0.57	0.01
2460304.977139	−76.70	4.99	−95.00	58.19	17.36	8.27	0.59	0.02
2460304.989955	−89.01	5.43	−78.90	68.27	−6.65	9.03	0.58	0.02
2460305.000413	−82.69	5.91	147.88	76.44	9.31	9.81	0.59	0.02
2460305.011955	−85.63	6.04	−115.77	78.04	13.34	10.03	0.60	0.02

Appendix B
Joint-fit Results

Figure 5 shows the posterior distributions of key parameters in the joint fit. Table B1 summarizes the prior settings and posteriors of other parameters except for those in Table 1.

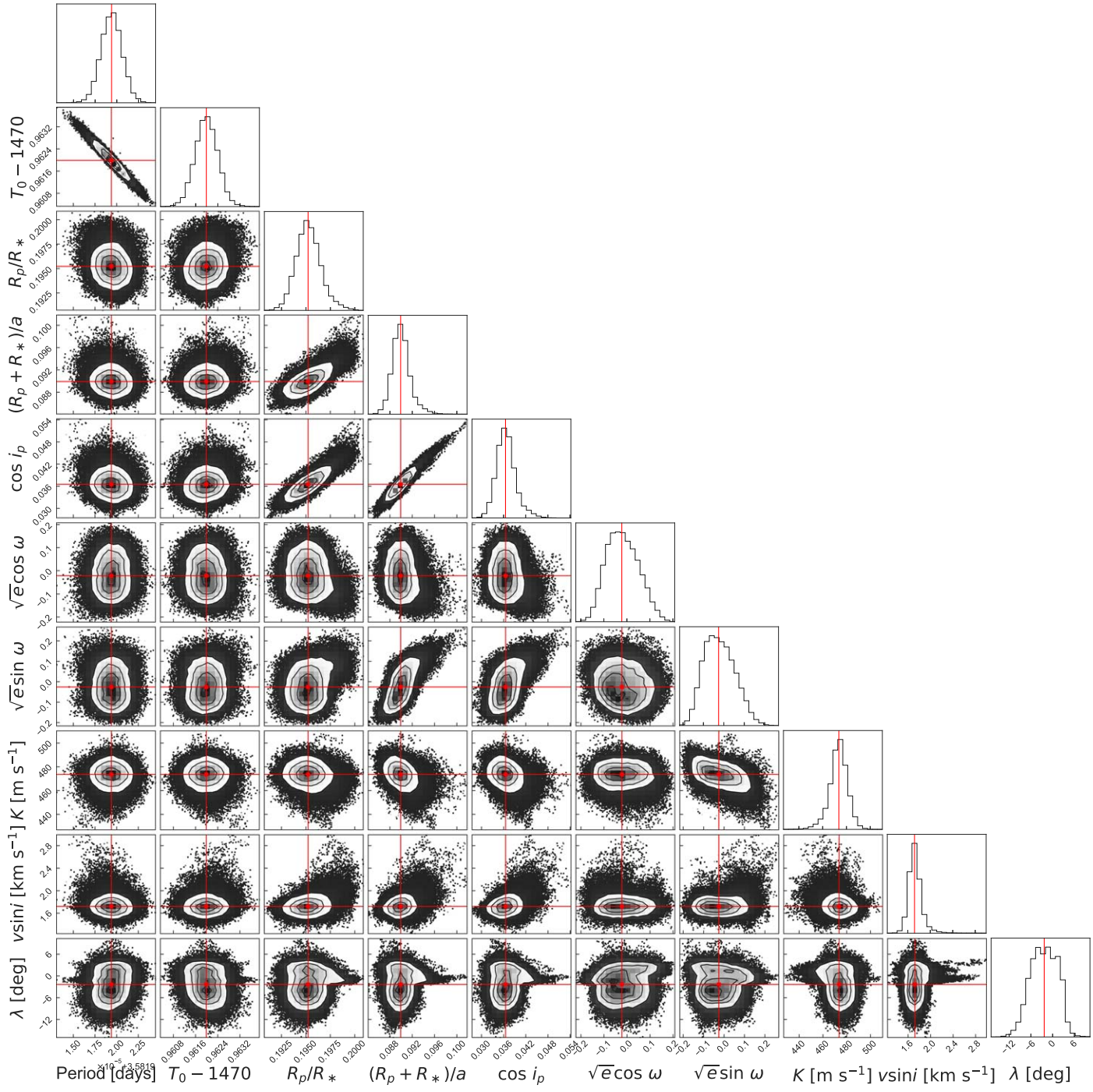

Figure 5. The posterior distributions of key parameters in the joint fit (see Section 3). The red solid lines mark the median values of each distribution.

Table B1
Priors and Best Fits of Other Parameters in the Joint Model

Parameter	Prior	Best Fit
Dilution factors		
$D_{\rm TESS\ S06}$	$\mathcal{TN}$ (0.1, 0.1^2,0,1)	$0.171^{+0.019}_{-0.020}$
$D_{\rm TESS\ S33}$	$\mathcal{TN}$ (0.1, 0.1^2,0,1)	$0.142^{+0.016}_{-0.015}$
$D_{\rm ground}$	0 (Fixed)	...
Limb-darkening Coefficients		
$q_{\rm 1,TESS\ S06}$	$\mathcal{U}$ (0,1)	$0.08^{+0.16}_{-0.08}$
$q_{\rm 2,TESS\ S06}$	$\mathcal{U}$ (0,1)	$0.67^{+0.32}_{-0.33}$
$q_{\rm 1,TESS\ S33}$	$\mathcal{U}$ (0,1)	$0.64^{+0.22}_{-0.20}$
$q_{\rm 2,TESS\ S33}$	$\mathcal{U}$ (0,1)	$0.15^{+0.33}_{-0.14}$
$q_{\rm LCO,SAAO,g}$	$\mathcal{U}$ (0,1)	$0.76^{+0.34}_{-0.32}$
$q_{\rm LCO,SAAO,i}$	$\mathcal{U}$ (0,1)	$0.31^{+0.23}_{-0.18}$
$q_{\rm LCO,CTIO,g}$	$\mathcal{U}$ (0, 1)	$0.73^{+0.09}_{-0.11}$
$q_{\rm LCO,CTIO,i}$	$\mathcal{U}$ (0, 1)	$0.29^{+0.10}_{-0.11}$
$q_{\rm MuSCAT,g}$	$\mathcal{U}$ (0, 1)	$0.55^{+0.06}_{-0.07}$
$q_{\rm MuSCAT,r}$	$\mathcal{U}$ (0, 1)	$0.62^{+0.03}_{-0.04}$
$q_{\rm MuSCAT,z}$	$\mathcal{U}$ (0, 1)	$0.33^{+0.04}_{-0.05}$
$q_{\rm SPECULOOS,z}$	$\mathcal{U}$ (0, 1)	$0.34^{+0.05}_{-0.06}$
Relative Photometric Offset		
$M_{\rm TESS\ S06}$	$\mathcal{U}$ (−1, 1)	$0.00013^{+0.00030}_{-0.00031}$
$M_{\rm TESS\ S33}$	$\mathcal{U}$ (−1, 1)	$0.00021^{+0.00023}_{-0.00022}$
$M_{\rm LCO,SAAO,g}$	$\mathcal{U}$ (−1, 1)	$0.00014^{+0.00226}_{-0.00219}$
$M_{\rm LCO,SAAO,i}$	$\mathcal{U}$ (−1, 1)	$0.00080^{+0.00085}_{-0.00084}$
$M_{\rm LCO,CTIO,g}$	$\mathcal{U}$ (−1, 1)	$-0.00039^{+0.00070}_{-0.00071}$
$M_{\rm LCO,CTIO,i}$	$\mathcal{U}$ (−1, 1)	$-0.00024^{+0.00054}_{-0.00051}$
$M_{\rm MuSCAT,g}$	$\mathcal{U}$ (−1, 1)	$0.00492^{+0.00032}_{-0.00033}$
$M_{\rm MuSCAT,r}$	$\mathcal{U}$ (−1, 1)	$0.00297^{+0.00016}_{-0.00017}$
$M_{\rm MuSCAT,z}$	$\mathcal{U}$ (−1, 1)	$0.00364^{+0.00014}_{-0.00013}$
$M_{\rm SPECULOOS,z}$	$\mathcal{U}$ (−1, 1)	$-0.00021^{+0.00021}_{-0.00020}$
Photometric Jitter		
$\ln\sigma_{\rm TESS\ S06}$	$\mathcal{U}$ (−15, 0)	$-5.99^{+0.09}_{-0.08}$
$\ln\sigma_{\rm TESS\ S33}$	$\mathcal{U}$ (−15, 0)	$-5.59^{+0.04}_{-0.03}$
$\ln\sigma_{\rm LCO,SAAO,g}$	$\mathcal{U}$ (−15, 0)	$-4.73^{+0.19}_{-0.16}$
$\ln\sigma_{\rm LCO,SAAO,i}$	$\mathcal{U}$ (−15, 0)	$-5.27^{+0.17}_{-0.16}$
$\ln\sigma_{\rm LCO,CTIO,g}$	$\mathcal{U}$ (−15, 0)	$-5.77^{+0.16}_{-0.14}$
$\ln\sigma_{\rm LCO,CTIO,i}$	$\mathcal{U}$ (−15, 0)	$-6.16^{+0.21}_{-0.15}$
$\ln\sigma_{\rm MuSCAT,g}$	$\mathcal{U}$ (−15, 0)	$-5.73^{+0.07}_{-0.06}$
$\ln\sigma_{\rm MuSCAT,r}$	$\mathcal{U}$ (−15, 0)	$-6.03^{+0.05}_{-0.04}$
$\ln\sigma_{\rm MuSCAT,z}$	$\mathcal{U}$ (−15, 0)	$-6.29^{+0.04}_{-0.04}$
$\ln\sigma_{\rm SPECULOOS,z}$	$\mathcal{U}$ (−15, 0)	$-5.51^{+0.04}_{-0.03}$
Relative RV Offset		
$\mu_{\rm HIRES}$ (m s^{-1})	$\mathcal{U}$ (−500, 500)	$3.0^{+14.3}_{-13.1}$
$\mu_{\rm NEID}$ (m s^{-1})	$\mathcal{U}$ (−500, 500)	$-288.1^{+40.6}_{-40.5}$
$\mu_{\rm PFS}$ (m s^{-1})	$\mathcal{U}$ (−500, 500)	$44.1^{+7.6}_{-7.7}$
$\mu_{\rm SPIRou}$ (m s^{-1})	$\mathcal{U}$ (−500, 500)	$-19.9^{+12.1}_{-12.0}$
$\mu_{\rm MAROON-X,Blue}$ (m s^{-1})	$\mathcal{U}$ (−500, 500)	$-1.5^{+4.4}_{-4.2}$
$\mu_{\rm MAROON-X,Red}$ (m s^{-1})	$\mathcal{U}$ (−500, 500)	$-4.8^{+4.2}_{-3.5}$
Spectroscopic Jitter		
$\ln\sigma_{\rm HIRES}$ (m s^{-1})	$\mathcal{U}$ (−15, 0)	$-2.9^{+0.4}_{-0.3}$
$\ln\sigma_{\rm NEID}$ (m s^{-1})	$\mathcal{U}$ (−15, 0)	$-8.3^{+2.3}_{-3.5}$
$\ln\sigma_{\rm PFS}$ (m s^{-1})	$\mathcal{U}$ (−15, 0)	$-3.6^{+0.4}_{-0.3}$
$\ln\sigma_{\rm SPIRou}$ (m s^{-1})	$\mathcal{U}$ (−15, 0)	$-3.0^{+0.3}_{-0.2}$
$\ln\sigma_{\rm MAROON-X,Blue}$ (m s^{-1})	$\mathcal{U}$ (−15, 0)	$-6.8^{+2.6}_{-4.8}$
$\ln\sigma_{\rm MAROON-X,Red}$ (m s^{-1})	$\mathcal{U}$ (−15, 0)	$-10.7^{+2.6}_{-4.0}$

Note. $\mathcal{TN}(\mu, \sigma^2, a, b)$ represents a truncated normal prior ranging from a to b.

ORCID iDs

Tianjun Gan https://orcid.org/0000-0002-4503-9705
Sharon X. Wang https://orcid.org/0000-0002-6937-9034
Fei Dai https://orcid.org/0000-0002-8958-0683
Joshua N. Winn https://orcid.org/0000-0002-4265-047X
Shude Mao https://orcid.org/0000-0001-8317-2788
Siyi Xu https://orcid.org/0000-0002-8808-4282
Enric Pallé https://orcid.org/0000-0003-0987-1593
Jacob L. Bean https://orcid.org/0000-0003-4733-6532
Madison Brady https://orcid.org/0000-0003-2404-2427
Nina Brown https://orcid.org/0009-0003-1142-292X
Cicero Lu https://orcid.org/0000-0001-9352-0248
Rafael Luque https://orcid.org/0000-0002-4671-2957
Teo Mocnik https://orcid.org/0000-0003-4603-556X
Andreas Seifahrt https://orcid.org/0000-0003-4526-3747
Guðmundur K. Stefánsson https://orcid.org/0000-0001-7409-5688

References

Addison, B. C., Horner, J., Wittenmyer, R. A., et al. 2021, AJ, 162, 137
Akeson, R. L., Chen, X., Ciardi, D., et al. 2013, PASP, 125, 989
Albrecht, S., Winn, J. N., Johnson, J. A., et al. 2012, ApJ, 757, 18
Albrecht, S. H., Dawson, R. I., & Winn, J. N. 2022, PASP, 134, 082001
Almenara, J. M., Bonfils, X., Forveille, T., et al. 2022, A&A, 667, L11
Baraffe, I., Homeier, D., Allard, F., & Chabrier, G. 2015, A&A, 577, A42
Barnes, S. A. 2007, ApJ, 669, 1167
Bean, J. L., Seifahrt, A., Hartman, H., et al. 2010, ApJ, 713, 410
Beck, J. G., & Giles, P. 2005, ApJL, 621, L153
Bellm, E. C., Kulkarni, S. R., Graham, M. J., et al. 2019, PASP, 131, 018002
Bourrier, V., Lovis, C., Beust, H., et al. 2018, Natur, 553, 477
Bourrier, V., Lovis, C., Cretignier, M., et al. 2021, A&A, 654, A152
Brady, M., Bean, J. L., Seifahrt, A., et al. 2023, AJ, 165, 129
Brown, D. J. A., Collier Cameron, A., Hall, C., Hebb, L., & Smalley, B. 2011, MNRAS, 415, 605
Bryant, E. M., Bayliss, D., & Van Eylen, V. 2023, MNRAS, 521, 3663
Chatterjee, S., Ford, E. B., Matsumura, S., & Rasio, F. A. 2008, ApJ, 686, 580
Dai, F., & Winn, J. N. 2017, AJ, 153, 205
Dai, F., Winn, J. N., Berta-Thompson, Z., Sanchis-Ojeda, R., & Albrecht, S. 2018, AJ, 155, 177
Dalal, S., Hébrard, G., Lecavelier des Étangs, A., et al. 2019, A&A, 631, A28
Dawson, R. I., & Johnson, J. A. 2018, ARA&A, 56, 175
Delamer, M., Kanodia, S., Cañas, C. I., et al. 2024, ApJL, 962, L22
Eastman, J., Siverd, R., & Gaudi, B. S. 2010, PASP, 122, 935
Engle, S. G., & Guinan, E. F. 2018, RNAAS, 2, 34
Fabrycky, D., & Tremaine, S. 2007, ApJ, 669, 1298
Ford, E. B., & Rasio, F. A. 2008, ApJ, 686, 621
Foreman-Mackey, D., Hogg, D. W., Lang, D., & Goodman, J. 2013, PASP, 125, 306
Gan, T., Cadieux, C., Jahandar, F., et al. 2023, AJ, 166, 165
Gan, T., Wang, S. X., Wang, S., et al. 2023a, AJ, 165, 17
Günther, M. N., & Daylan, T. 2021, ApJS, 254, 13
Hartman, J. D., Bakos, G. Á., Csubry, Z., et al. 2023, AJ, 166, 163
Hébrard, G., Ehrenreich, D., Bouchy, F., et al. 2011, A&A, 527, L11
Hirano, T., Gaidos, E., Harakawa, H., et al. 2024, MNRAS, 530, 3117
Hirano, T., Gaidos, E., Winn, J. N., et al. 2020a, ApJL, 890, L27
Hirano, T., Krishnamurthy, V., Gaidos, E., et al. 2020b, ApJL, 899, L13
Kipping, D. M. 2013, MNRAS, 435, 2152
Kraft, R. P. 1967, ApJ, 150, 551
Lai, D. 2012, MNRAS, 423, 486
Libby-Roberts, J. E., Schutte, M., Hebb, L., et al. 2023, AJ, 165, 249
Mamajek, E. E., & Hillenbrand, L. A. 2008, ApJ, 687, 1264
Martioli, E., Hébrard, G., Moutou, C., et al. 2020, A&A, 641, L1
Masci, F. J., Laher, R. R., Rusholme, B., et al. 2019, PASP, 131, 018003
Masuda, K., & Winn, J. N. 2020, AJ, 159, 81
Mayor, M., & Queloz, D. 1995, Natur, 378, 355
McLaughlin, D. B. 1924, ApJ, 60, 22
Naoz, S. 2016, ARA&A, 54, 441
Palle, E., Oshagh, M., Casasayas-Barris, N., et al. 2020, A&A, 643, A25

Petrovich, C., Muñoz, D. J., Kratter, K. M., & Malhotra, R. 2020, ApJL, 902, L5
Pinsonneault, M. H., DePoy, D. L., & Coffee, M. 2001, ApJL, 556, L59
Rasio, F. A., & Ford, E. B. 1996, Sci, 274, 954
Ricker, G. R., Winn, J. N., Vanderspek, R., et al. 2015, JATIS, 1, 014003
Rossiter, R. A. 1924, ApJ, 60, 15
Rubenzahl, R. A., Dai, F., Howard, A. W., et al. 2021, AJ, 161, 119
Sanchis-Ojeda, R., & Winn, J. N. 2011, ApJ, 743, 61
Sanchis-Ojeda, R., Winn, J. N., Holman, M. J., et al. 2011, ApJ, 733, 127
Schlaufman, K. C. 2010, ApJ, 719, 602
Seifahrt, A., Bean, J. L., Stürmer, J., et al. 2020, Proc. SPIE, 11447, 114471F
Seifahrt, A., Stürmer, J., Bean, J. L., & Schwab, C. 2018, Proc. SPIE, 10702, 107026D
Spalding, C., & Winn, J. N. 2022, ApJ, 927, 22
Stefansson, G., Mahadevan, S., Maney, M., et al. 2020, AJ, 160, 192
Stefànsson, G., Mahadevan, S., Petrovich, C., et al. 2022, ApJL, 931, L15
Wang, S., Winn, J. N., Addison, B. C., et al. 2021, AJ, 162, 50
Winn, J. N., Fabrycky, D., Albrecht, S., & Johnson, J. A. 2010, ApJL, 718, L145
Winn, J. N., & Fabrycky, D. C. 2015, ARA&A, 53, 409
Wu, Y., & Lithwick, Y. 2011, ApJ, 735, 109
Zahn, J. P. 1977, A&A, 57, 383
Zechmeister, M., Reiners, A., Amado, P. J., et al. 2018, A&A, 609, A12